

Advanced Noise Control Fan Direct Aeroacoustics Predictions using a Lattice-Boltzmann Method

Adrien Mann¹, Franck Pérot², Min-Suk Kim³,
Exa Corporation, 150 North Hill Drive, Brisbane, CA, 94005, USA

Damiano Casalino⁴, Ehab Fares⁵
Exa GmbH, Curiestrasse 4, Stuttgart, 70563, Germany

A Lattice-Boltzmann Method (LBM) based approach is used to perform transient, explicit and compressible CFD/CAA simulations on the Advanced Noise Control Fan (ANCF) configuration. The complete 3-D ducted rotor/stator model including all the geometrical details and the truly rotating rotor is simulated. Detailed near and far-field measurements conducted at the NASA Glenn research center are used to validate the simulation results. The measured and predicted sound pressure levels at the far-field microphones are compared and both show the presence of broadband noise and sharp peaks which frequencies depend on the number of rotor blades and the angular velocity of the rotor. The 3-D duct acoustics modes observed in experiments are also captured in the 3-D transient CFD/CAA calculation and detailed analyses of the results are presented. The main circumferential modes predicted from the number of rotor blades and stator vanes are recovered in both experimental and simulation modal decompositions.

Nomenclature

M	=	Mach number
f_k	=	k^{th} BPF harmonic order
c_b	=	Rotor blade chord
s_b	=	Rotor blade span
Δx_{tip}	=	Tip clearance
c_v	=	Stator vane chord
$d_{h,up}$	=	Upstream hub diameter
$d_{h,do}$	=	Downstream hub diameter
p	=	Static pressure
r	=	Radial coordinate
θ	=	Azimuthal coordinate
x	=	Axis coordinate
t	=	Time
m	=	Circumferential mode order
n	=	Radial mode order
k	=	x -axis eigenvalue
κ	=	radial eigenvalue
J_m	=	Bessel function of the first kind and order m
B	=	Number of fan blades
V	=	Number of stator vanes
s	=	Fan shaft harmonic
Ω	=	Rotation frequency of the fan
c_0	=	Speed of sound

¹ Aeroacoustics engineer, Aeroacoustics Applications, amann@exa.com, AIAA Member

² Director, Aeroacoustics Applications, perot@exa.com, AIAA Member

³ Senior aeroacoustics engineer, Aeroacoustics Applications, mskim@exa.com

⁴ Principal Aeroacoustics engineer, Aerospace Applications, damiano@exa.com, AIAA Member

⁵ Technical Manager, Aerospace Applications, ehab@exa.com, Senior AIAA Member

R_0	=	Fan radius
ρ_0	=	Air density
C_i	=	Discrete collision component in the i^{th} direction
c_i	=	Discrete velocity component in the i^{th} direction
f_i	=	Particle distribution function in the i^{th} direction
T	=	Temperature
τ	=	Relaxation time
ν	=	Kinematic viscosity
Δt	=	Numerical time step

I. Introduction

Aeroacoustic noise generated by turbofan engines especially during take-off conditions, when engines are operating at high throttle settings, is still a major noise source of annoyance and significantly contributes to community noise issues in the vicinity of airports. Several noise reduction programs in the United States such as the Advanced Subsonic Technology (AST) and the Quiet Aircraft Technology (QAT), as well as the European ACARE “Visions 2020” set challenging targets for the aerospace industry such as reducing the overall perceived noise impact of future aircraft by one half within the coming ten years. Major developments of noise reduction concepts applied to various noise contributors such as airframe and engine are therefore expected to be of crucial importance to the aerospace industry in order to fulfill future certification targets and satisfy customers and community expectations.

One component of turbofan noise is the flow-induced contribution caused by the rotor-stator system. Significant overall broadband levels are radiated to the far field due to motion and stretching of turbulent flow eddies^{1,2}. In addition, generally intense tonal noise at specific frequencies as a result of rotor-stator interaction coupled with duct mode propagation in the nacelle is observed²⁻⁹. In the past decade, an effort towards the development of efficient acoustics liner aiming to reduce mainly the tonal part of the noise has been carried out. Optimization algorithms, based on the modal decomposition of the sound pressure propagation, help improve and accelerate the design of such efficient liners^{10,11}. A method allowing accurate modal decomposition as well as a good estimation of overall broadband content is therefore required. The Advance Noise Control Fan (ANCF) geometry of the NASA Glenn Research Center was developed in the early 1990’s to provide detailed measurements of a turbo fan flow and corresponding noise produced by the ducted rotor/stator^{2-9,12,13}. The measurements provide a better understanding of the correlation between the flow and the propagation inside the duct as well as the radiation to the far field. The facility also allows the physical testing of innovative concepts and the evaluation of the efficiency of future technologies, such as optimized acoustic liners. In an effort to help the development and validation of aerodynamics and aeroacoustic solvers, the extensive datasets and the published geometry are made available to the scientific and engineering community^{2,3,14-16}.

Numerous efforts in order to predict the modal content of the propagated flow and understand the noise generation mechanisms led to the development of analytical models of turbofans^{17,18,19}. But an accurate and quantitative prediction of all noise produced by the rotor/stator interaction remains a challenging and daunting task. In the present study, transient and compressible direct aeroacoustics computations are performed on the ANCF geometry. These simulations aim at correctly predicting the tonal noise as well as the broadband content. The rotor rotation is truly simulated in the Computational Fluid Dynamics/Computational Aeroacoustics (CFD/CAA) simulations using a Local Reference Frame (LRF) approach. The self-noise in the nacelle together with the radiated acoustic field are recovered from the solely compressible CFD/CAA simulations based on the Lattice Boltzmann Method (LBM). The focus of this study is the comparison of the simulated results to the detailed far-field noise measurements, to identify the origin of the tonal content and to make the link between the flow-induced noise sources with the duct modes. Analytical derivations presented in previous studies are also used to discuss the predicted results.

In a first section, a description of the experimental setup is presented including the overview of the modal decomposition and the presentation of the rotating rake, a device designed for extracting the modal content of pressure fluctuations. In a second section, a detailed presentation of the numerical setup is given, including the numerical method, the simulation details and the modal post-processing. In a last part, detailed analyses of the aerodynamic properties of the flow, of the radiated far-field noise and of duct modes pinpoint the mechanisms of noise source generation in the ducted turbofan.

II. Experimental setup

A. Measurements description

Geometry and Conditions

The ANCF geometry depicted in Fig. 1 is a configurable 4 foot diameter ducted fan installed in the hemispherical anechoic test facility of the Aero-Acoustics Propulsion Laboratories at the NASA Glenn Research Center. The 16-bladed rotor operating condition varies from 100 *rpm* to 2400 *rpm* and the nominal value is 1800 *rpm*. The inlet duct Mach number due to the mass flow induced by the turbofan is $M \sim 0.15$. The fundamental Blade Passing Frequency (BPF) is $f_0 = 480$ Hz. The geometry can be installed such that only the rotor is present with an adjustable fan blades pitch of 18° - 38° (nominally 28°). The blade chord is $c_b = 133.4$ mm and the span is $s_b = 580.4$ mm. The very small tip clearance is $\Delta x_{tip} \sim 0.76$ mm. The stator hub has a variable blade count and can be installed at

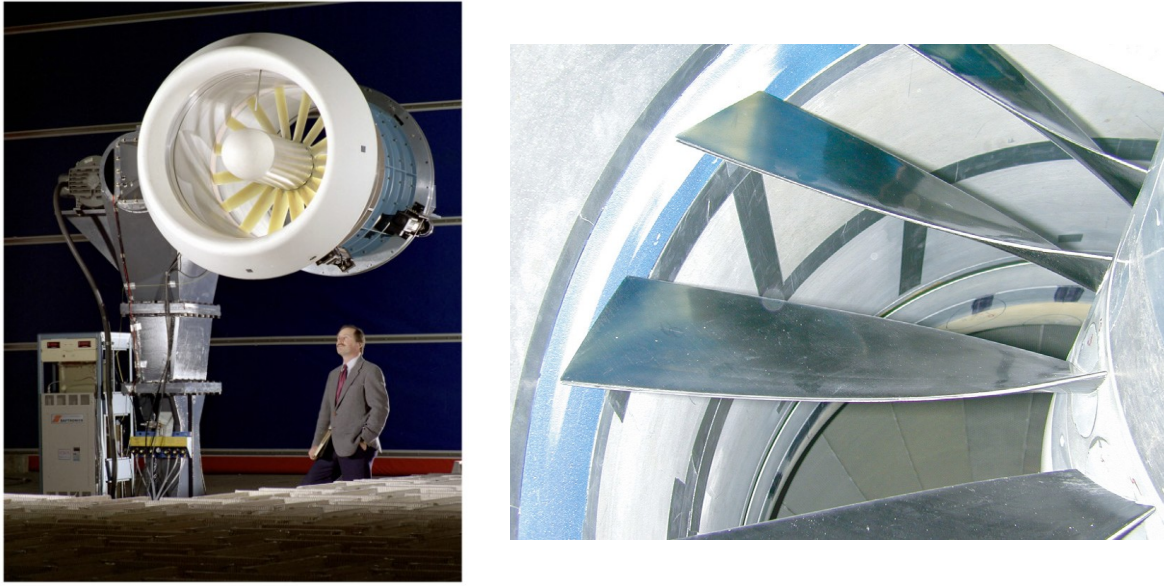


Figure 1. Advanced Control Fan Geometry (left) and the installed rotor blade geometry (right)

any pitch angle. Each stator vane chord is $c_v = 114.3$ mm. Further details about the geometry are documented in several publications^{2,3,14-16}. The rotor/stator configuration simulated in this study is based on the nominal fan conditions and a 13-vane stator located one stator chord downstream the rotor. The hub diameter is $d_{h,up} = 457.2$ mm at the fan and $d_{h,do} = 609.6$ mm at the exhaust.

Available Far Field Acoustic Measurements

Thirty far-field microphones arranged in two semicircular arcs centered on the duct inlet and outlet, at a 12-feet distance are recording the noise, as depicted in Fig. 2. Signal sampling is performed synchronously and 256 samples per fan revolution are acquired¹⁵ for about 20 seconds. Tones Power Levels (PWL) are computed from the measured Sound Pressure Level (SPL) at the BPFs up to the 6th fan harmonics for each microphone. Other dynamic and static pressure probes are also available in the measurements^{14,15}. More recent measurements¹⁴ include flow characterizations using hot-film anemometer as well as dedicated aerodynamic performance measurements¹⁶ including further static and total pressure probe rakes allowing mass flow as well as shaft axial velocities measurements. The nominal geometry setup uses a 13 vanes configuration for the stator, for which noise measurements are available.

B. Rotating rake for modal analysis

In order to capture the modal decomposition of pressure fluctuations in the duct, a unique innovative system called rotating rake has been developed². Using the properties of the duct modes behavior and based on the Doppler Effect, it allows performing modal analysis without disturbing the flow from the introduction of microphones across the duct.

Modal decomposition

The propagation of sound in a circular duct in the presence of a uniform flow satisfies the convective wave equation. In cylindrical coordinates (r, θ, x) , this equation writes as follows:

$$\Delta^2 p(r, \theta, x, t) = \left(\frac{\partial}{\partial t} + M \frac{\partial}{\partial x} \right)^2 p(r, \theta, x, t) \quad (1)$$

A general form of the solution, propagating in only one direction, is a projection of the real solution on an infinite set of functions, at time frequency f :

$$p(r, \theta, x, t) = p_{mnf} * E_{mn}(\kappa_{mn}r) e^{i(2\pi ft + m\theta - \kappa_{mn}x)} \quad (2)$$

with

$$E_{mn}(\kappa_{mn}r) = C_{mn}[J_m(\kappa_{mn}r) + Q_{mn}Y_m(\kappa_{mn}r)] \quad (3)$$

Equation 3 is a linear combination of Bessel functions of the first kind J_m and second kind Y_m of order m . The circumferential m -order is the representation of the periodicity in pressure along the circumferential θ direction. The radial n -order defines the number of pressure nodes along the radial r -direction. The weighting factor C_{mn} normalizes the arbitrary Bessel function profile to a desired physical property. It is chosen so that the averaged pressure power on each section of the cylinder is equal to its surface area. In the case of a cylindrical duct, with no hub, Eqs (2) and (3) simplify to:

$$E_{mn}(\kappa_{mn}r) = C_{mn} * J_m(\kappa_{mn}r) \quad (4)$$

$$\frac{1}{C_{mn}^2} = \frac{1}{2} \left(1 - \frac{m^2}{\kappa_{mn}^2} \right) J_m^2(\kappa_{mn}) \quad (5)$$

The radial eigenvalues κ_{mn} are obtained with the boundary conditions written at the outer wall:

$$\frac{dP}{dr}(r = R) = 0 \rightarrow \kappa_{mn} \frac{J_{m+1}(\kappa_{mn})}{J_m(\kappa_{mn})} - m = 0 \quad (6)$$

For a given circumferential mode m , Eq. (6) has an infinite number of solutions. Since these values are all real and positive, they can be ordered and define the n -radial mode order as the position of κ_{mn} in this ordered set. n also indicates the number of pressure nodes, *i.e.* the number of times the pressure changes sign along the radius. A description of the mode structure is given in Fig. 3.

The axial eigenvalue k_{mn} defines the ability of a given mode (m, n) to propagate along the x -axis. The solution of the propagation equation in the x -direction gives²:

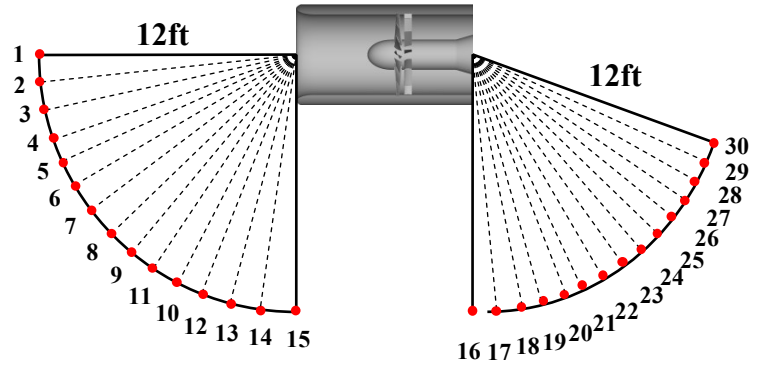


Figure 2. Thirty Microphones located in the far-field

$$k_{mn} = \frac{\eta}{1-M^2} \left[-M \pm \sqrt{1 - (1-M^2) \left(\frac{\kappa_{mn}}{\eta} \right)^2} \right] \text{ with } \eta = \frac{2\pi f R_0}{c_0} \quad (7)$$

The eigenvalue k_{mn} is real if the real number κ_{mn} is small enough compare to η , i.e. $(\kappa_{mn}/\eta)^2 > 1/(1-M^2)$. The corresponding modes n , at a given mode m , define the cut-on modes. Outside of this range, the imaginary part of k_{mn} is non zero and a decay of the corresponding pressure mode is observed along x . This range corresponds to the cut-off modes. Cut-on modes propagate in the duct introducing a periodicity along x whereas cut off modes decay and progressively disappear from the noise content. All cut-on modes propagate with a helix shape², except $m=0$.

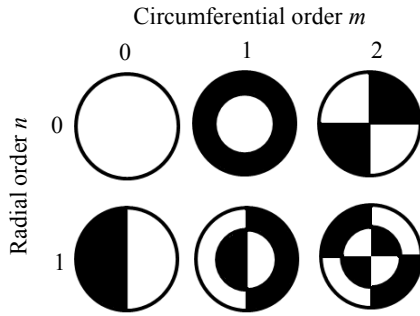


Figure 3. Duct mode representation

Since only a finite subset of modes is able to propagate, the number of terms in Eq. (2) has been limited. However, the higher the frequency, the higher the possible value of n as shown with Eq. (7). The number of possible modes can thus become large. The published work of Tyler and Sofrin²⁰ helps reducing this number. Only modes m corresponding to specific linear combinations of the number of rotor blades B and of the number of stator vanes V are actually dominant in the source region. The common expression for these modes is as follows:

$$m = sB \pm kV \text{ with } (s, k) \in \mathbb{Z} \times \mathbb{N} \quad (8)$$

Each propagating mode spins at $\Omega_m = sB\Omega/m$ and the relationship between the BPF harmonics and the shaft harmonic order s is given by $f_{BPF} = |sB\Omega|$. More details on the modal decomposition in duct geometries are given by Sutliff.

Rotating rake implementation

In order to perform the modal decomposition of sound pressure waves in the duct, at a given x , an intuitive way of extracting pressure p utilizes a cylindrical coordinates-based array of microphones. However, the number of microphones needed to capture all the m -modes participating in the propagation in the duct up to the 3rd BPF harmonic would be twice the maximum value of m . For example, if the maximum number is 15 as given by Sutliff², more than 30 microphones for each radial position r are needed in order to recover the periodicity along θ . If the expected number of n -modes is 5, more than 150 microphones would have to be equally distributed along θ and r in the duct. Such a web array would cause disturbances in the flow that are likely to affect the behavior of the rotor-stator noise generation. This method is however used for the simulation as no flow contamination is introduced.

In order to limit the perturbation of the flow, a rotating rake system has been developed based on the Doppler Effect. Given Eq. (2), if one microphone rotates at a low angular velocity Ω_θ , the measured pressure sustains at each m -mode a unique shift in frequency due to the Doppler Effect. The observed frequency at this probe is:

$$f' = \Omega \left(sB - \frac{m}{v} \right) \quad (9)$$

with v an integer and $\Omega / \Omega_\theta = 1/v$. The value of the pressure at each frequency is computed from a Fast Fourier Transform (FFT) along the time dimension, and each major peak, obtained at different values of f' , corresponds to a unique couple (f, m) in the rotating rake frame of reference. This system limits the intrusion in the flow to only one rotating linear rake. Six to seven microphones are evenly distributed along the rake for the computation of the n -modes².

The various effect and pollution induced by this device are explained by Sutliff² while presenting the modal analysis results obtained from the ANCF rotating rake extracted data. Modal pressure is obtained though post processing and modal power can then be computed from the following equation:

$$P = \mp \frac{\pi R^2}{\rho_0 c_0} |\beta|^4 \text{Re} \left(\frac{\alpha_{mns}}{|1 \pm M \alpha_{mns}|^2} \right) |p|^2 \quad (10)$$

$$\text{with } \beta = \sqrt{1 - M^2}, \alpha_{mns} = \sqrt{1 - \frac{1}{\zeta_{mns}^2}} \text{ and } \zeta_{mns} = \frac{2\pi s B \Omega R_0}{\kappa_{mn} c_0}.$$

III. Simulation Setup

A. Simulation description

Lattice Boltzmann Method overview

The CFD/CAA solver PowerFLOW 4.3 based on the Lattice Boltzmann Method (LBM) is used to calculate unsteady flow physics and the corresponding flow-induced noise generation and radiation. Lattice-based methods are by nature explicit, transient and compressible, and are an alternative to traditional CFD methods based on the discretization of the Navier-Stokes equations and derived variations.

The LBM is based on the velocity space discretization of the Boltzmann equation to predict macroscopic fluid dynamics. The lattice Boltzmann equation has the following form:

$$f_i(\mathbf{x} + \mathbf{c}_i \Delta t, t + \Delta t) - f_i(\mathbf{x}, t) = C_i(\mathbf{x}, t) \quad (11)$$

with f_i the particle distribution function moving in the i^{th} direction, according to a finite set of discrete velocity vectors $\{\mathbf{c}_i; i=0,..b\}$, $\mathbf{c}_i \Delta t$ and Δt are respectively space and time increments. For convenience, we choose the convention $\Delta t=1$ in the following discussions. The collision term on the right hand side of Eq. (11) adopts the form known as the Bhatnagar-Gross-Krook (BGK)²¹⁻²³:

$$C_i(\mathbf{x}, t) = -\frac{1}{\tau} [f_i(\mathbf{x}, t) - f_i^{eq}(\mathbf{x}, t)] \quad (12)$$

with τ the relaxation time parameter, and f_i^{eq} the local equilibrium distribution function, which depends on local hydrodynamic properties. The basic hydrodynamic quantities, such as fluid density ρ and velocity \mathbf{u} , are obtained through moment summations:

$$\rho(\mathbf{x}, t) = \sum_i f_i(\mathbf{x}, t), \quad \rho \mathbf{u}(\mathbf{x}, t) = \sum_i \mathbf{c}_i f_i(\mathbf{x}, t) \quad (13)$$

For a suitable choice of the set of discrete velocity vectors, the transient compressible Navier-Stokes equations are recovered through Chapman-Enskog expansion, in the limit of low Mach numbers, *i.e.* $M < 0.5$. The resulting equation of state obeys the ideal gas law, and the kinematic viscosity of the fluid is related to the relaxation time parameter τ as documented by Shan and Chen²⁴, Li et al.²⁵ and Chen et al.²⁶. The combination of Equations (11) to (13) forms the usual LBM scheme for fluid dynamics, which is solved on a grid composed of cubic volumetric elements called voxels. In the code used for this study, a Variable Resolution (VR) strategy is employed, where the grid size changes by a factor of two for adjacent resolution regions²⁷.

In order to model the effects of unresolved small scale turbulent fluctuations, the lattice Boltzmann equation is extended by replacing its molecular relaxation time scale with an effective turbulent relaxation time scale, *i.e.* $\tau \rightarrow \tau_{eff}$, where τ_{eff} is derived from a systematic Renormalization Group (RG) procedure detailed by Chen et al.^{26,27}. This method is commonly called Very Large Eddy Simulation (VLES) and is now validated and productively used for solving a large range of problems related to aerodynamics, convective heat transfer and aeroacoustics²⁸⁻³⁵.

Fan rotation implementation

For simulations of flows with arbitrary geometry rotating in time around a fixed axis, the 3-D dimensional computational domain is divided into an inner and an outer domain. The inner domain has a grid fixed with the rotating geometry so that the geometry does not have a relative motion with respect to the grid. This forms a “body-fixed” Local Reference Frame (LRF) domain with the rotating geometry³⁶. The grid in the outer domain is fixed with the ground and forms a “ground-fixed” reference frame domain. Between the inner domain and outer domain, there is a closed transparent interface to connect fluid flows. Additional details on the numerical implementation are given by Pérot *et al*^{37,38,39} and Pérot *et al*^{40,42}. Many results for the application of LRF method have been published^{42,43,44}.

Geometry and numerical aspects

As shown in Fig. 4, the complete geometry, i.e. rotor, stator, hub and duct are included in the simulation. The rotor/stator configuration simulated in this study is based on the nominal fan conditions: 1800 *rpm*, 16-blade, 13-vane, 28° rotor pitch angle and stator located one stator chord downstream the rotor. The tip clearance of the fan is not considered in the simulation and set to $\Delta x_{tip}=0$ *mm*. The geometry is embedded into a large anechoic simulation domain. Symmetric boundary conditions are used on all the external boundaries. This choice was made for simplicity and due to the large size of the simulation volume. The finest grid resolution used around the rotor and stator is $\Delta x=1.5$ *mm* corresponding to about 800 voxels across the nacelle diameter. An overview of the grid is given in Fig. 4. The model size is 1.62×10^8 voxels.

The simulation time step is $dt=2.44 \times 10^{-6}$ *s* and the calculation is performed over a period $T=0.6$ *s* of physical time corresponding to 18 complete rotor rotations. The resolution at the far-field microphones is $\Delta x_{mic}=12$ *mm* and assuming 16 points per wave length necessary to propagate acoustics waves with minimum dissipation, the estimated grid cut-off frequency is $f_{cut} \sim 2500$ *Hz*. For performing the flow and modal analyses, the instantaneous pressure, velocity components and the density are recorded on various surfaces and volumes at a high frequency rate during 6 rotations. The calculation time is about 450 CPU-h per rotation on a 128 AMD 2.2 GHz Dual Core Opteron processors clusters.

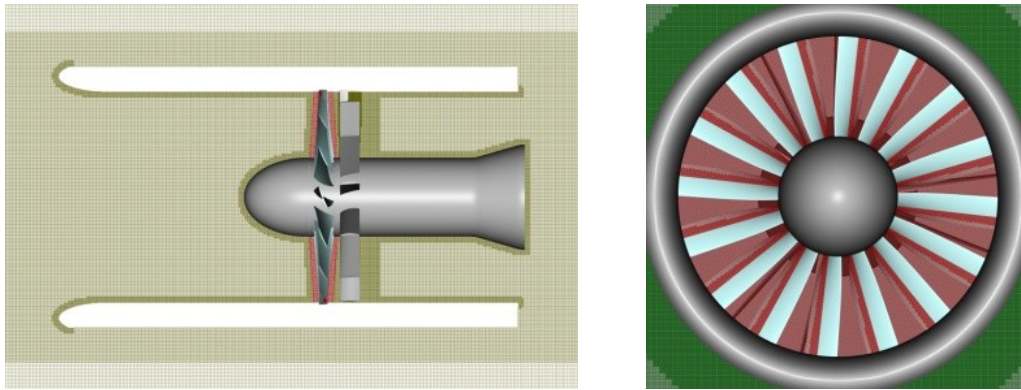


Figure 4. Simulated ANCF geometry and grid overview. The resolution in the red and dark green areas is 1.5mm. The entire simulation domain is not represented and the red area corresponds to the rotation region (LRF).

B. Modal decomposition method

After the simulation, the modal analysis of the pressure in the duct is performed. Pressure is first extracted on a (r, θ) spider-web shaped grid from a high frequency sampling measurement plane. The spider-web is composed of 6001 extraction nodes evenly distributed on a disk. Resolution is fixed to $res_{\theta}=120$ points along in the azimuthal θ -direction and $res_r=51$ points in the radial r -direction including $(0,0)$. Following Eq. (2), the modal decomposition of sound pressure is obtained from the discrete Fourier Transform of the recorded signal in time and θ -angle domain and its projection on the system of Bessel Function of the first kind (J_m).

As a first step of the procedure, a time FFT is performed at each signal providing complex pressure $p(r, \theta)$. Figure 5 illustrates the Root Mean Square (RMS) pressure obtained from this operation. Local maxima of pressure corresponding to BPF harmonics f_0, f_1 and f_2 are extracted, as well as any other chosen value f . These frequencies are generated by the rotor system as follows¹³:

$$f_i = (i + 1)\Omega B \quad (14)$$

Next, a θ -FFT of complex pressure $p(r, \theta)$ is performed in order to obtain the circumferential modes m . The data from the previous calculation is first improved by artificially lengthening the pressure signals. The signal is by geometrical consideration 2π -periodic and is repeated a hundred times. This method improves the result of the θ -FFT accuracy by narrowing the pressure peaks. An example of the θ -FFT result obtained with the improved signal $p'_i(r, \theta)$ at the outer wall is presented in Fig. 5.

The last step is the computation of n -modes with a least square method. This method computes the modal pressures p_{mnf} by minimizing the difference between calculated and analytical pressure:

$$\delta^2 = \left(\sum_{n=0}^{N_{max}} p_{mnf} E_{mn}(\kappa_{mn} r) - p_m(r) \right)^2 \quad (15)$$

The maximum value of radial modes is set to $N_{max}=11$, more than twice the maximum cut-on mode n at the 3rd BPF harmonic according to Sutliff. The minimization is achieved by cancelling each derivative of δ^2 according to p_{mnf} values:

$$\frac{\partial \delta^2}{\partial p_{mnif}} = 0 \quad (16)$$

Details of the method are given by Sutliff² with an emphasis on the mathematical formulation of the algorithm. The corresponding modal power P_{mnf} is obtained from Eq. (10). As explained in the previous section, cut-off modes are disregarded from the modal decomposition.

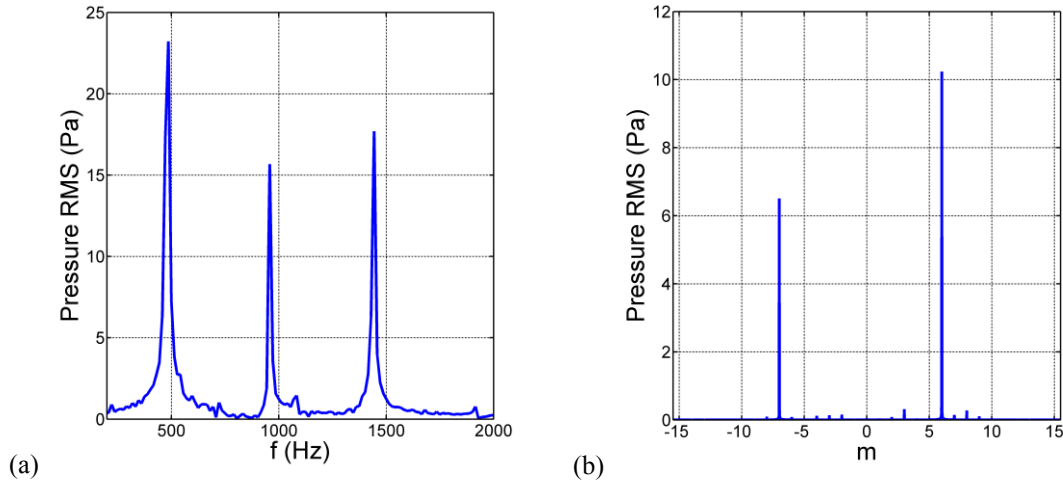


Figure 5. RMS value of the complex pressure. Time-FFT of one probe in the extraction web at $r=R_0$ (a) and θ -FFT as a function of the circumferential order m (b).

IV. Aerodynamics and aeroacoustics analyses

A. Instantaneous flow analysis

Instantaneous flow results are extracted from the simulation and averaged results from the transient flow are compared to published data of the ANCF experiment. The main flow of the 13 vanes-ANCF configuration aerodynamics results have however not been published by NASA yet and a comparison is made with the 14 vanes configuration instead¹⁶. Averaged total pressure is presented in Fig. 7. The simulation is underestimating by 35Pa the experiment close to $r=254\text{mm}$ and matches it close to the wall of the duct at $r \approx 609\text{mm}$. The simulated geometry does not include the Inlet Control Device (ICD) described by Bozak¹⁶ which result in a 35Pa drop in the pressure in the duct at the nominal conditions. It is therefore a possible explanation for the observed difference. The simulated mass flow is 48.6kg/s and underestimates the measured mass flow by 7.5%, a value generally observed in fan simulations.

The turbulent structure of the flow is depicted in Fig. 8 with the representation of the isosurface of λ_2 -coefficient⁴⁵. Turbulent structures at the rotor-stator are observed downstream the fan and are source of propagated noise in the duct. Vortices are also present at the exhaust where a shear layer is produced by the difference in velocity between the ejected flow and the mean flow. This turbulent flow generates noise and contributes to the

broadband levels in spectra. Velocity magnitude, vorticity magnitude and static pressure are captured in the simulation and presented on a y -plane across the duct in Fig. 6. The turbulent part of the flow downstream the exhaust is generated within the shear layers. A ring-shape plume containing multiple scales of eddies is visible on each plot. Acoustic radiation propagates from the duct extremities and the turbulent jet and a pressure drop in the duct due to the fan is present as illustrated by the static pressure plot. A periodic pattern in velocity magnitude and vorticity magnitude is observed downstream the stator and illustrates the blade passage effect on the instantaneous flow.

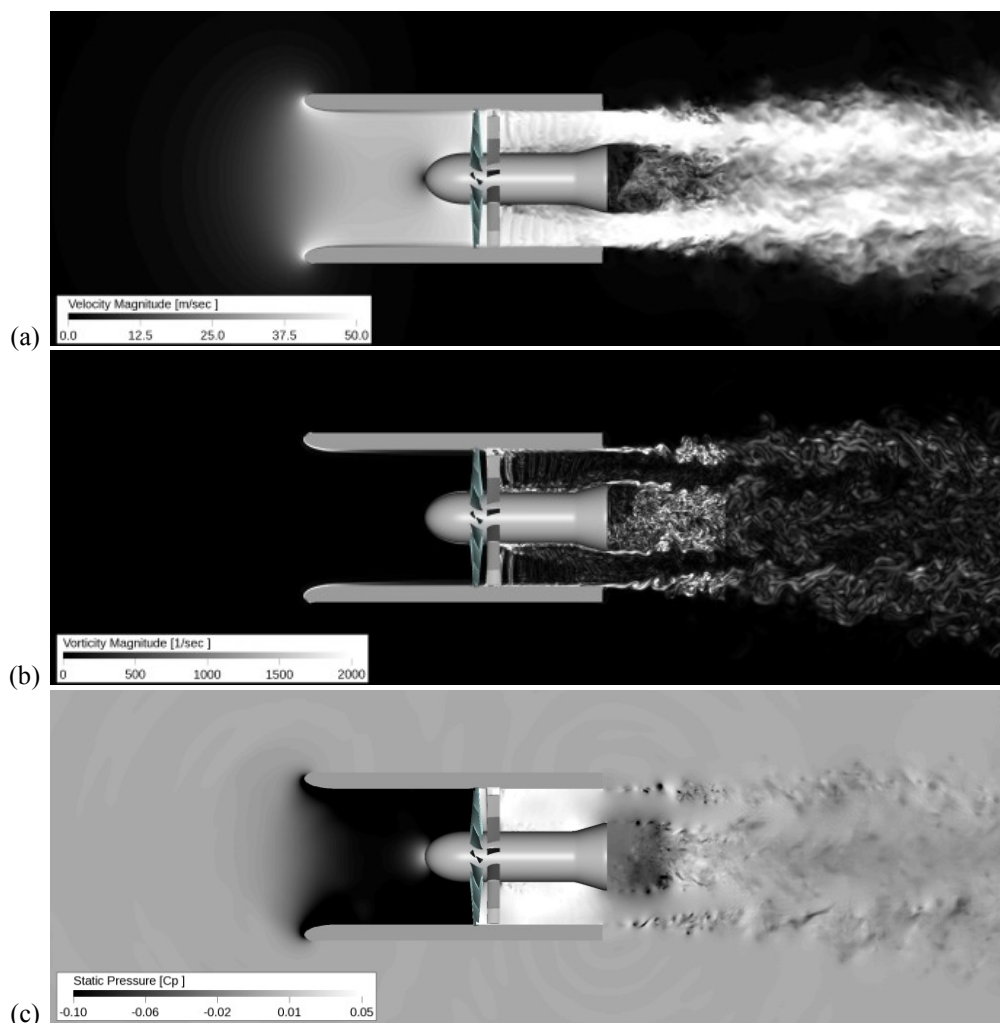


Figure 6. Instantaneous velocity (a), vorticity (b) and pressure (c) from simulation.

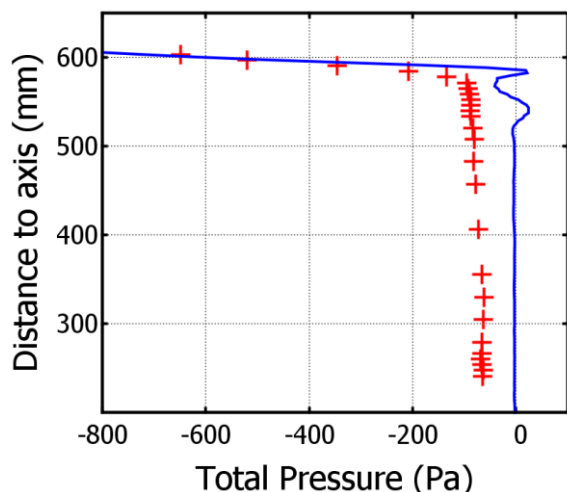


Figure 7. Total pressure at the inlet for the experiment (red) and the simulation (blue)

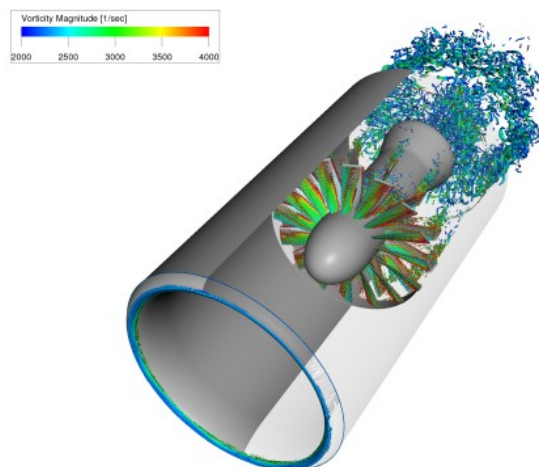


Figure 8. Instantaneous flow field represented with the λ_2 -coefficient⁴⁵ isosurface colored by the

B. Far-field Sound Pressure Levels

In Fig. 8, Sound Pressure Levels (SPL) from the simulation (blue) and experiments (red) are represented at four microphone locations. Microphones numbers are 4, 11, 20 and 26 (see Fig. 2). The distance between the microphones and the rotor is twelve feet and the predicted SPLs are obtained directly from the transient and compressible simulation. As expected, the cut-off frequency of the simulation is about 2-3 kHz and could be improved by increasing the grid resolution between the ANCF and the far-field microphones. The three first BPF frequencies at $f_0=480\text{Hz}$, $f_1=960\text{Hz}$ and $f_2=1440\text{Hz}$ are accurately captured in the simulation and the broadband levels are also in good agreement. In Fig. 9, the directivity of the SPLs from the simulation (left) and experiments (right) are represented. In the diagram, the radial coordinate is the frequency f and the angle coordinate is the angular position of the microphones (see Fig. 2). The first three BPF are captured in the simulation, as well as the broadband levels, especially at frequencies up to 1.5 kHz upstream and downstream. For angles between 60° and 120° these levels are well captured up to 2 kHz. The first and second BPF values are in good agreement upstream and downstream. The simulation is overestimating the 3rd BPF by 20 dB downstream for angles close to 90° . The general trend is an underestimation of the broadband levels by about 5dB to 10dB compared to experiment and an agreement to BPFs levels within 5dB except in a few directions, such as the range 90° - 120° at the 3rd BPF.

In Fig. 10, directivity diagrams corresponding to the OASPL, computed on the 100Hz-2kHz band, and to the first three BPFs are plotted. The OASPL are captured within 5-10 dB upstream and 3-5 dB downstream. The shape of the directivity plot is in reasonable agreement with the experiments, confirming observations from Fig. 9. In the first BPF directivity diagram, the upstream SPL values are over-predicted by 5-10 dB in the simulation, and the downstream values are in excellent agreement within 2-4 dB except at one microphone off by 10 dB at 65° . The second BPF directivity plot is the best in terms of levels and diffraction patterns. Predicted SPLs match the experiment results upstream the fan within 4 dB in average and 7 dB downstream. The third BPF diagram is showing an overestimation of the SPL value by up to 20 dB, also depicted in Fig. 9. Upstream SPL are overall matching experiment data within 10dB.

SPLs at angles between 60° and 120° correspond to sound waves originating from the diffraction of duct modes at the inlet and at the exhaust. Results in this area are sensitive to the geometry and missing details or parts can explain the discrepancy. A complete description of the ANCF facility is available in publications^{14,15} for comparison. The absence of tip clearance and outlet shaft are also good candidates to explain the differences.

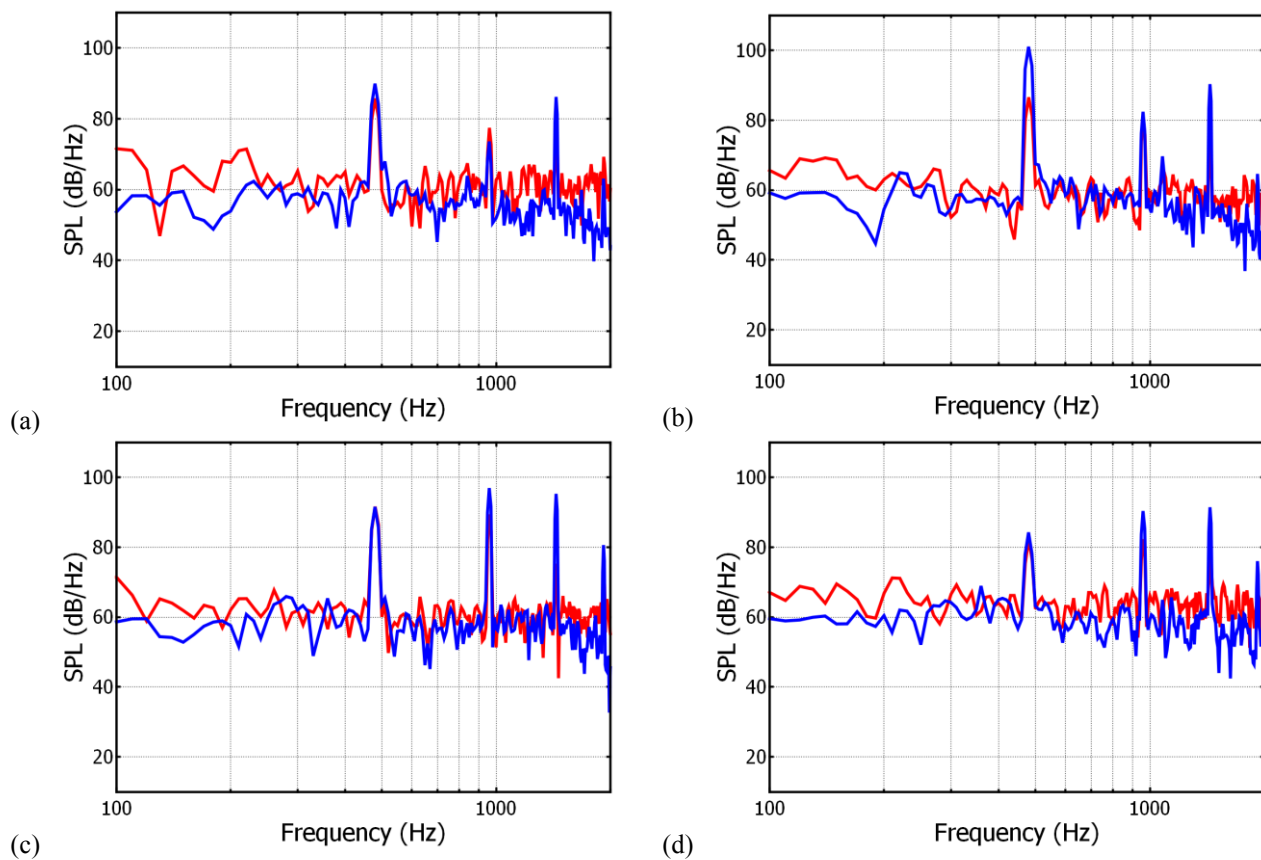


Figure 8. SPL of microphones 4, 11, 20 and 26 from (a) to (d). (—) Experiment and (—) simulation results.

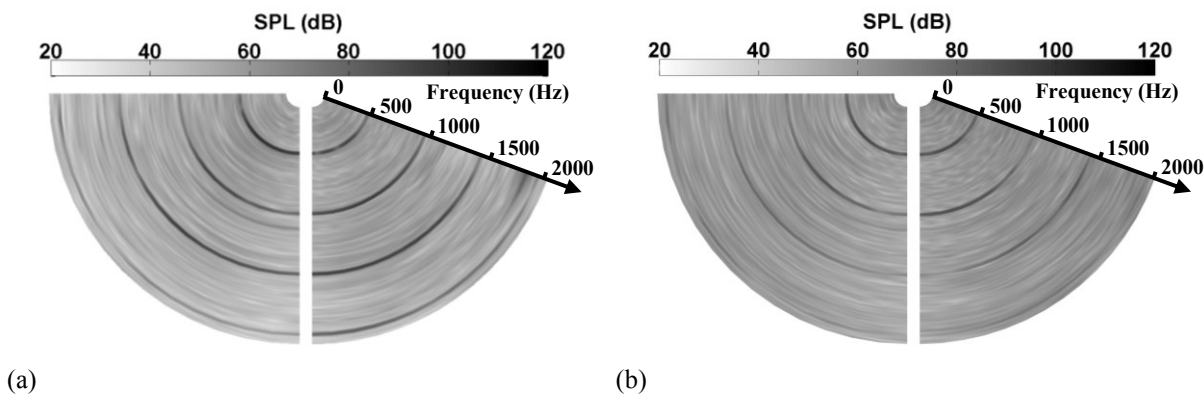


Figure 9. SPL of microphones as a function of the position angle and frequency. Simulation (a) and experiment (b) results.

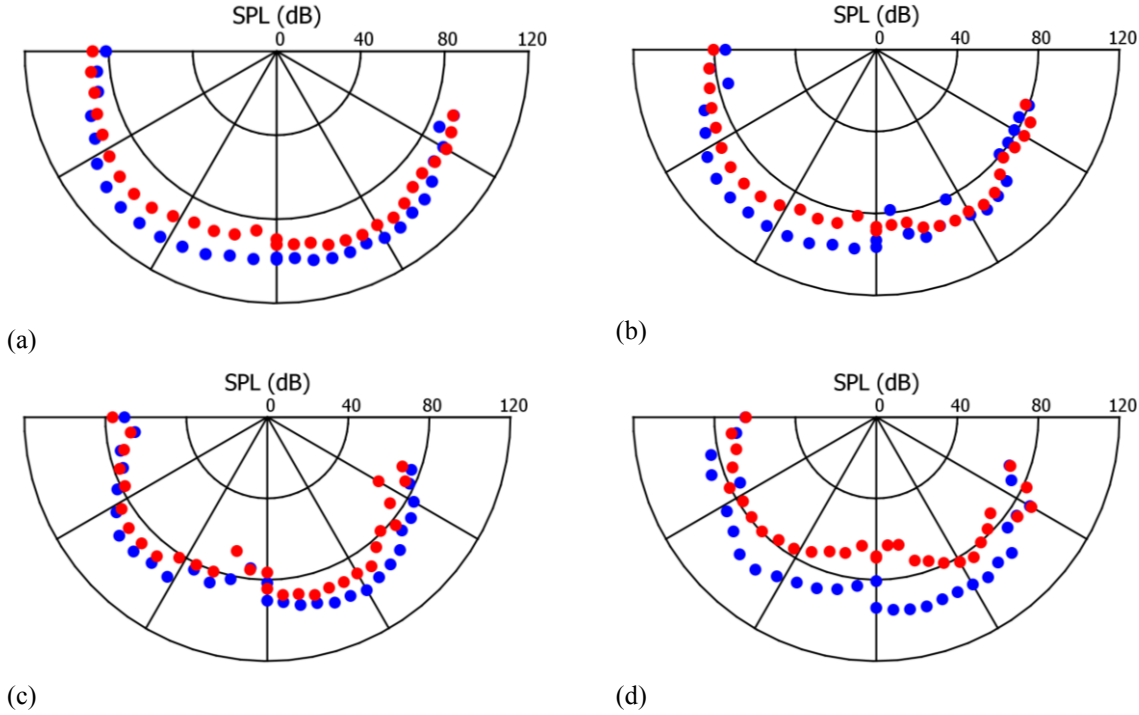


Figure 10. Directivity plot corresponding to OASPL, f_0 , f_1 and f_2 . Experiment (red) and simulation (blue)

C. Band-filtered pressure

With an access to the transient pressure information at each time step and each location of space, the predicted mode patterns can be observed in the simulation by visualizing the narrow band filtered pressure in the time domain around the different BPFs. Combinations of the dominant modes are directly visible as depicted in Fig. 13. The band-filtered pressure extracted from 20 Hz range bands centered on f_0 , f_1 and f_2 , from top to bottom, is represented on the surface of the geometry (left) and on a y-plane across the geometry (right). At the first BPF order, the helix-shape propagation of dominant mode (3,0) is captured on the surface (see section D). Diffraction patterns and directivity are directly observable on the y-plane, as well as the propagation of modes in the duct for all three frequencies. Diffracted sound waves from the exhaust, (respectively from the inlet) contribute to the upstream microphones SPLs (respectively to the downstream microphones). It confirms that if the exterior geometry close to the inlet and outlet surface is not fully accurate, discrepancies are likely to be observed. The number of energized modes at the third BPF is larger than at the first and second BPF, and the consequent interference between dominant modes is characterized by the complexity of the pressure fluctuations inside the duct, as presented in Fig 11.c. The convection of the turbulent eddies downstream the geometry explains the specific pattern observed on the plane downstream the exhaust of the ANCF. Results are obtained simultaneously with the flow results without any coupled acoustics solver.

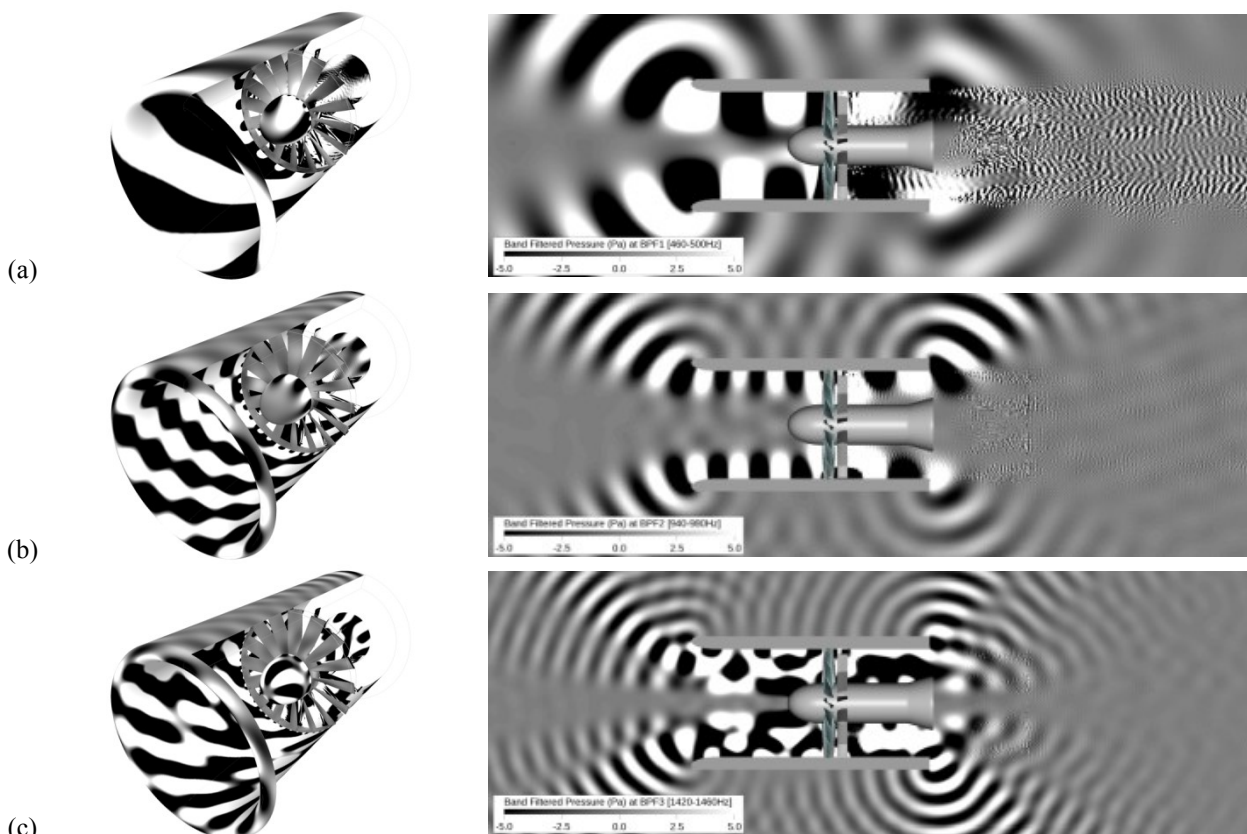


Figure 11. Band filtered pressure at the surface (left) and on a plane (right) for frequencies f_0 , f_1 and f_2 from (a) to (c).

D. Duct modes analysis at BPF harmonic orders

As described by Tyler and Sofrin²⁰, and shown in Eq. (8), the rotor-stator interaction energizes a limited number of (m,n) combinations at each BPF. The range of n and m is set by the cut-off/cut-on boundary as described in Eq. (7). The ducted turbofan only produces sound waves at few values of m -order. For example, at the first BPF, the subset of propagating modes (m,n) is illustrated by the pyramidal shape of cut-on PWL depicted in Fig. 12. Since the shaft harmonic order at f_0 is $s=1$, Eq. (8) states that the ducted rotor/stator interaction generates only the m -order $m_0=1 \times 16 - 1 \times 13 = 3$. At f_1 , the fan shaft harmonic order is equal to $s=2$, and the system mainly generates m -order $m_1=-7$ and $m_1=6$. At f_2 , the fan shaft harmonic order is equal to $s=3$, and the system mainly generates m -order $m_2=-4$ and $m_2=9$. The modal decomposition of each BPF harmonic f_0 , f_1 and f_2 respectively from left to right are depicted in Fig. 12 for the experiment (a.) and the simulation (b.) in which modal power is plot as a function of m and n . In Table 1, the values of PWL for the main combinations of m and n are extracted. For the first BPF harmonic, the simulation is underestimating the single dominant peak value at $(m,n)=(3,0)$ by 2 dB. Other levels from the simulation, called secondary modes, are up to 30dB lower than the experiment. The PWL levels in the experiment are all within 5 dB of the average value 82dB except main mode (3,0). Fluctuations of the secondary modes in the simulation are larger, within 15 dB of the average value 65 dB. Characteristics of the experimental setup or differences in the post-processing method are good candidates to explain the overall higher results of the experiment. For example, the microphones wake noise can contribute to the secondary modes excitation. The discrepancies are currently investigated with NASA in order to determine the origins of this modal background noise. At the second BPF, the simulation dominant PWL for combination $(-7,0)$ is overestimating the experiment by 4 dB, whereas combination $(6,0)$ is underestimated by 1.5 dB. The same behavior as for the first BPF order is observed for secondary combinations in the experiment. Fluctuations of power in secondary modes are within 20 dB of the average value 78dB in the experiment. In the simulation, fluctuations are within 30 dB of the average value 55 dB. The average secondary modes power is lower in the simulation, but again the fluctuations are larger band.

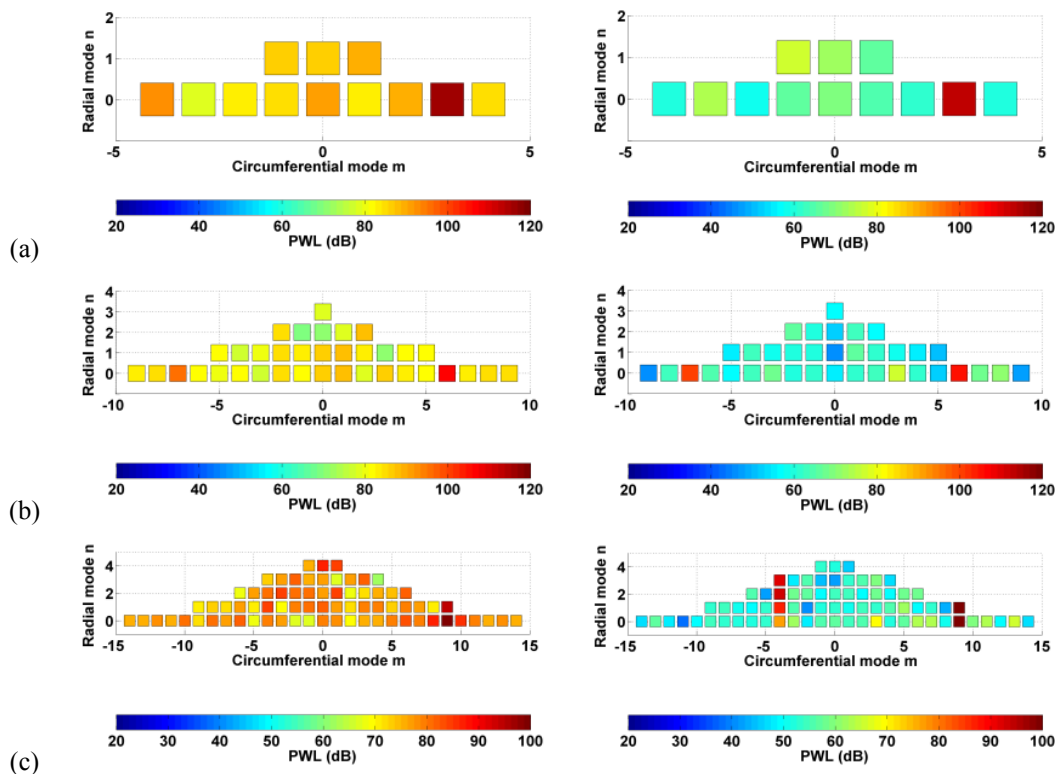


Figure 12. PWL as a function of m and n . Left: experiments; Right: Simulation. (a) to (c): $f_0=480$ Hz, $f_1=980$ Hz and $f_2=1440$ Hz.

Discrepancies between simulation and experiment at the third BPF order are larger. Combinations of modes (9,0) and (-4,1) are off by less than 3 dB, but the strongest mode for the simulation is observed at mode (9,0) and is overestimating the experiment results by 10 dB. The same order of difference is observed for the mode (-4,2). Mode (-4,3) is overestimated by the simulation by 18 dB. The absence of tip clearance in the simulation can explain the difference on these specific modes modifying the boundary layer tip interaction mechanism. Fluctuations of secondary levels are still within a 10 dB range centered on the average value for the experiment. Simulation secondary PWLs are unevenly distributed in modal space within a 30 dB range centered on the average value. If the tip clearance can justify the differences for the dominant modes, the discrepancy in behavior at secondary levels is likely to be explained by the background noise in the experiment or the post-processing treatment applied to signals. The analysis is extended for all frequencies between 100 Hz and 2 kHz. For each frequency, the modal analysis is performed and the complex pressures at modes (m,0) are computed. The corresponding SPLs are presented on Fig. 13 at two different locations in the flow. The first location is at the inlet (left), the same as the rotating rake position in the experiment. The second web location is 612 mm upstream the rotor. Since Eq. (10) is not applied, all modes (m,0) are plotted, including cut-off modes. According to Eq. (7), the number of cut-on modes increases with the frequency. Consequently, a triangular boundary between cut-on and cut-off modes at $n=0$ as observed is expected. Cut-off modes correspond to the blue area of the diagram. Maximum values of SPL are obtained at BPF harmonic orders energized by mechanisms occurring at the rotor/stator, and at m -orders corresponding to Tyler and Sofrin²⁰

Table 1. PWL (dB) for expected combinations of m and n at 1st, 2nd and 3rd BPF harmonic order

BPF	Frequency (Hz)	(m,n)	Experiment (dB)	Simulation (dB)
1 st	480	(3,0)	115.4	113.0
2 nd	960	(-7,0)	96.4	100.3
		(6,0)	106.9	105.2
		(-4,1)	83.9	86.9
		(-4,2)	81.0	92.9
3 rd	1440	(-4,3)	73.7	91.3
		(9,0)	101.0	100.4
		(9,1)	94.8	104.5

predictions (Eq. (8)). The decay of the cut-off modes is also illustrated by the change in color outside of the triangle from blue at the hub (right) to dark blue at the inlet (left). The vertical lines in the diagram illustrate a distribution of energy along specific values of m . This pattern in the graph is currently under investigation. Since a decay of these lines is observed in the cut-off modes area, these modes may originate from upstream and may be generated by the rotor/stator interaction and/or the eddies fluctuations at the exhaust. The rotor/stator system might somehow influence broadband noise levels.

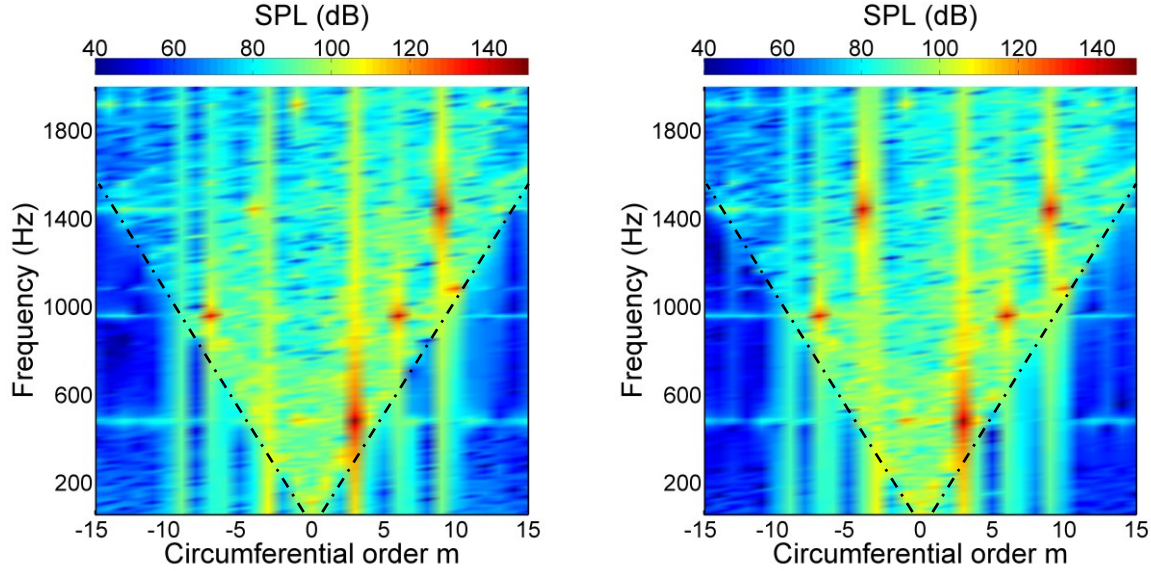


Figure 13. Modal SPL as a function of m and f at $n=0$. Modes computed at the inlet web (left) and at the hub web (right).

In Table 2 and 3, Instantaneous pressure fields are reconstructed at f_0 and f_2 using spider-webs shape grid at the inlet and close to the extremity of the hub. For the experiments, only the pressure at the inlet is presented. The reconstruction is performed using the band-filtered pressure on a plane at the inlet, the full cut-on modal decomposition, and the main cut-on modes identified from Fig. 12 and predicted by Eq. (8). Since the cut-off modes decay along the x -direction, the cut-on based reconstruction must have the same pattern as the band-filtered results. The main modes simulation must also be similar to the band-filtered pressure distribution pattern. At first BPF harmonic, the mode (3,0) is dominant and no difference in pressure distribution between band-filtered pressure, cut-on modes and main modes reconstructions, both at the inlet, are visible from the simulation results. Only a phase shift in the θ -direction is observed explained by the spinning nature of the sound wave propagation. Experiment results at the inlet are different, due to the influence of the flat background noise distributed on all secondary cut on modes. However, when the main mode (3,0) is isolated, no difference is observed with simulation results. At the third BPF harmonic, observations are similar for the first BPF between band-filtered signal, cut-on based and main reconstructions at the inlet and at the hub. The difference in pressure distributions between the inlet and the hub web cannot be explained by a phase shift only. The change in level of the mode (-4,3) between the hub and the inlet can explain the difference. If the cut-on based reconstruction is performed with a decreased level at (-4,3) mode, the pressure distribution pattern is similar to the observed pattern at the inlet. The loss of energy of this particular mode in the simulation can be explained by the proximity of mode (-4,3) to the cut-on/cut-off boundary (see Fig. 12). The analytical solution predicts no decay but the simulation may give a non-zero imaginary part for the x -eigenvalue λ_{mn} by introducing a shift in the cut-on/cut-off boundary. A new simulation setup allowing the decomposition of the pressure fluctuations in the simulation in the x -direction would give insight into the problem. The spinning speed and direction of the different modes is illustrated in time animations of the band-filtered results. The central pattern at the third BPF indeed rotates in one direction, due to mode (-4,3) and (-4,2), and in the opposite direction close to the duct walls due to modes (9,0) and (9,1). This behavior as well as a difference in rotation speed is noticed in these animations.

Table 2. Pressure at the inlet and at the hub at f_0 obtained directly from the simulation by filtering the pressure field (left column), reconstructed from the cut-on modes (center column) and from dominant modes (right column)

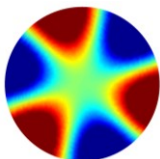
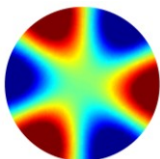
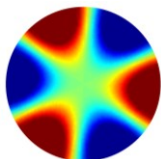
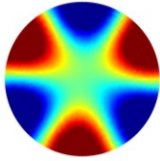
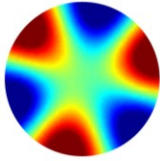
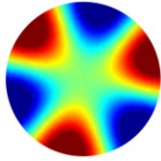
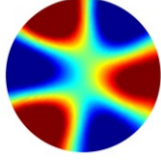
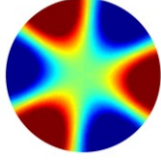
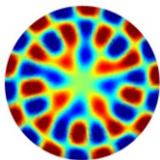
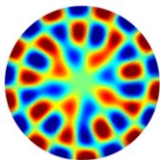
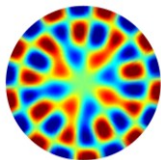
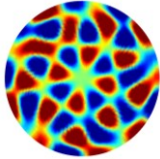
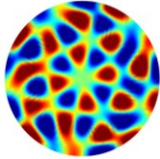
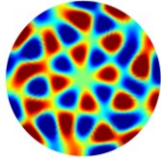
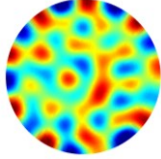
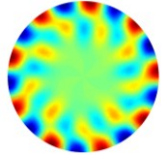
<i>Origin</i>	<i>Band filtered around f</i>	<i>Reconstructed from cut on modes</i>	<i>Reconstructed from main modes</i>
Simulation at the inlet			
Simulation at the hub			
Experiment at the inlet	<i>N.A.</i>		

Table 3. Pressure at the inlet and at the hub at f_2 obtained directly from the simulation by filtering the pressure field (left column), reconstructed from the cut-on modes (center column) and from dominant modes (right column)

<i>Origin</i>	<i>Band filtered around f_2</i>	<i>Reconstructed from cut on modes</i>	<i>Reconstructed from main modes</i>
Inlet web			
Hub web			
Experiment	<i>N.A.</i>		

V. Conclusions

This paper presents direct aeroacoustics predictions of the ANCF with comparison to detailed experimental measurements taken at the NASA Glenn Research center. Simultaneous flow and acoustics predictions are obtained using a LBM-VLES method, with the real rotation of the fan simulated using a Local Reference Frame approach. The numerical results favorably compare to experiments for both mean and fluctuating flow. The far field acoustic spectra show good agreement with measurements and capture correctly the blade passing frequencies as well as the broadband levels up to the cut-off frequency of the simulation. The simulation also captures the duct modes derived theoretically and observed experimentally. The simulation is used for investigating the instantaneous flow topology and for making the link between flow structures and related aeroacoustics field.

Far field acoustic predictions can also be obtained from the simulation at larger distances using a Ffowcs-Williams & Hawkings (FWH) algorithm. Results can then be part of a complete digital aircraft noise certification including an Effective Perceived Noise Level (EPNL) analysis⁴⁶. Future work will include the study of different mean flow configuration⁴⁷ with the analysis of the impact of inlet flow conditions and yawed geometry on noise. The effects of the number of blades/vanes of the stator/rotor as well as of the presence of a tip clearance will be investigated. The results of the modal analysis will ultimately be coupled with an acoustic liner optimization algorithm. The true geometry of the optimized acoustic liner will then be embedded to the ANCF geometry and simulated for the validation of the method.

VI. Acknowledgments

The authors are grateful to Daniel L. Sutliff at NASA Glenn Research Center for providing the geometry and the detailed experimental data needed for the validation.

References

- ¹ Ashtley, J. "Predicting and treating fan and turbomachinery noise: Current technology, research and facilities", Aircraft Emissions and Noise, 2006.
- ² Sutliff, D.L., Rotating "Rake Turbofan Duct Mode Measurement System", NASA TM-2005-213828, 2005.
- ³ Sutliff, D., Curtis, A., Heidelberg, L., and Remington, P. J., "Performance of Active Noise Control System for Fan Tones Using Vane Actuators", AIAA Paper No. 2000-1906, 6th AIAA/CEAS Aeroacoustics Conference, 2000.
- ⁴ Ganz, U. W., Joppa, P. D., Patten, T. J., and Scharpf, D. F., "Boeing 18-Inch Fan Rig Broadband Noise Test", Tech. Rep. CR-1998-208704, NASA, 1998.
- ⁵ Podboy, G. G. and Helland, S. M., "Fan Noise Source Diagnostic Test-Two-Point Hot-Wire Results", AIAA Paper No.2002-2431, 8th AIAA/CEAS Aeroacoustics Conference, 2002.
- ⁶ Woodward, R. P., "Fan Noise Source Diagnostic Test-Farfield Acoustic Results", AIAA Paper No. 2002-2427, 8thAIAA/CEAS Aeroacoustics Conference, 2002.
- ⁷ Premo, J., "Fan Noise Source Diagnostic Test-Circumferential Mode Measurements", AIAA Paper No. 2002-2429, 8th AIAA/CEAS Aeroacoustics Conference, 2002.
- ⁸ Envia, E., "Fan Noise Source Diagnostic Test-Vane Unsteady Pressure Results", AIAA Paper No. 2002-2430, 8th AIAA/CEAS Aeroacoustics Conference, 2002.
- ⁹ Heidelberg, L. J., "Fan Noise Source Diagnostic Test-Tone Modal Structure Results", AIAA Paper No. 2002-2428, 8th AIAA/CEAS Aeroacoustics Conference, 2002.
- ¹⁰ Lester H. C., Posey, J. W., "Duct Liner Optimization for Turbomachinery Noise Sources", NASA, TM-X-72789, 1975.
- ¹¹ Lafronza, L., McAlpine, A., Keane A. J., Astley, R., J., "Response Surface Method Optimization of Uniform and Axially Segmented Duct Acoustics Liners", Journal of Aircraft, Vol. 43, No. 4, pages 1089-1102, 2006.
- ¹² Moore, C.J., "Measurements of Radial and Circumferential Modes in Annular and Circular Ducts", Journal of Sound and Vibration, Vol. 62, No. 2, 1979.
- ¹³ Meyer, H.D., Envia, E., "Aeroacoustic Analysis of Turbofan Noise Generation", NASA, CR-4715, 1996.
- ¹⁴ McAllister, J., Lowe, R.A., Lauer, J.T., Sutliff, D.L., "The Advanced Noise Control Fan Baseline Measurements", AIAA Paper No. 2009-0624, 2009.
- ¹⁵ Loew, R.A., Lauer, J.T., McAllister and Sutliff, D.L., "The Advanced Noise Control Fan", AIAA Paper No. 2006-3150, also NASA TM-2006-214368, 2006.

- ¹⁶ Bozak, R.F., "Advanced Noise Control Fan Aerodynamic Performance", NASA TM-2009-215807, 2009.
- ¹⁷ Rice, E.J., Heidmann, M.F., Sofrin, T.G., "Modal Propagation Angles in a Cylindrical Duct with Flow and Their Relation to Sound Radiation", AIAA 97-0183, 1997.
- ¹⁸ Nallasamy, M. and Envia, E., "Computation of rotor wake turbulence noise", Journal of Sound and Vibration, Vol. 282, pp. 649-678, 2005.
- ¹⁹ Grace, S.M, Sondak, D.L., Eversman, W., and Cannamela, M.J., "Hybrid Prediction of Fan Tonal Noise", AIAA Paper No. 2008-2992, 2008.
- ²⁰ Tyler, J.M., Sofrin, T.G., "Modal Propagation Angles in a Cylindrical Duct with Flow and their Relation to Sound Radiation", AIAA Paper No. 97-0813, 1997.
- ²¹ Frisch, U., Hasslacher, B. and Pomeau, Y., 1986, "Lattice-gas Automata for the Navier-Stokes Equations," Phys. Rev. Lett., Vol. 56, pp.1505-1508.
- ²² Bhatnagar, P., Gross, E. and Krook, M., 1954, "A model for collision processes in gases. I. small amplitude processes in charged and neutral one-component system", Phys. Rev., vol.94, pp.511-525, 1954.
- ²³ Chapman, S. and Cowling, T., 1990, "The Mathematical Theory of Non-Uniform Gases", Cambridge University Press, 1990.
- ²⁴ Shan, X. and Chen, H., 1993, "Lattice Boltzmann model for simulating flows with multiple phases and components", Phys. Rev. E, 47, 1815-1819.
- ²⁵ Li, Y., Shock, R., Zhang, R., and Chen, H., 2004, "Numerical Study of Flow Past an Impulsively Started Cylinder by Lattice Boltzmann Method" J. Fluid Mech., Vol. 519, pp. 273-300.
- ²⁶ Chen, H., Orszag, S., Staroselsky, I. and Succi, S., 2004, "Expanded Analogy between Boltzmann Kinetic Theory of Fluid and Turbulence", J. Fluid Mech., Vol. 519, pp. 307-314.
- ²⁷ Chen, H., Kandasamy, S., Orszag, S., Shock, R., Succi, S. and Yakhot, V., "Extended Boltzmann Kinetic Equation for Turbulent Flows", Science, Vol. 301, pp. 633-636, 2003.
- ²⁸ Keating, A., Dethioux, P., Satti, R., Noelting, S., Louis, J., Van de Ven, T., and Vieito, R., 2009, "Computational Aeroacoustics Validation and Analysis of a Nose Landing Gear", AIAA 2009-3154, 13th AIAA/CEAS aeroacoustics conference, Miami, FL.
- ²⁹ Satti, R., Li, Y., Shock, R., Noelting, S., 2008, "Aeroacoustics Analysis of a High Lift Trapezoidal Wing using Lattice Boltzmann Method", AIAA-2008-3048, 12th AIAA/CEAS aeroacoustics conference, Vancouver, Canada.
- ³⁰ Adam, J.L., Ricot, D., Dubief, F., Guy, C., 2008, "Aeroacoustic Simulation of Automotive Ventilation Outlets", Proc. Acoustics '08 Conference, Paris, June 29.
- ³¹ Senthoooran, S., Crouse, B, Balasubramanian, G., Freed D., Shin S.R. and Ih K.D., 2008, "Effect of Surface Mounted Microphones on Automobile Side Glass Pressure Fluctuations", Proc. 7th MIRA Intl. Vehicle Aerodynamics Conf., Richoh Arena, UK, Oct.22.
- ³² Brès, G.A., Pérot, F., Freed, D., 2009, "Properties of the Lattice-Boltzmann Method for Acoustics", AIAA 2009-3395, 13th AIAA/CEAS aeroacoustics conference, Miami, Florida.
- ³³ Laffitte, A., Pérot, F, 2009, "Investigation of the Noise Generated by Cylinder Flows Using a Direct Lattice-Boltzmann Approach", AIAA 2009-3268, 13th AIAA/CEAS aeroacoustics conference, Miami, Florida.
- ³⁴ Pérot, F., Meskine, M., and Vergne S., 2009, "Investigation of the Statistical Properties of Pressure Loadings on Real Automotive Side Glasses", AIAA paper 2009-3402, 13th AIAA/CEAS aeroacoustics conference, Miami, Florida.
- ³⁵ Pérot, F., Kim, M.S., D.M. Freed, Dongkon, L., Ih, K.D., Lee, M.H., 2010a, "Direct aeroacoustics prediction of ducts and vents noise", AIAA paper 2010-3724, 14th AIAA/CEAS aeroacoustics conference, Stockholm, June.
- ³⁶ Hoch, J., 2004, "Rotating Reference Frames in PowerFLOW", Exa Corporation Internal Memorandum.
- ³⁷ Pérot, F., Moreau, S., Kim, M.S., Neal, D., "Investigation of the Flow Generated by an Axial 3-Blade Fan", 13th ISROMAC 2010-082, April 2010
- ³⁸ Pérot, F., Moreau, S., Henner, M., Neal, D. and Kim, M. "Direct Aeroacoustic Prediction of a Low-Speed Axial Fan", AIAA paper 2010-3887, 2010.
- ³⁹ Pérot, F., Wada, K., Norisada, K., Kitada, M., Hirayama, S., Sakai, M., Imahigasi, S., Sasaki, N., "HVAC Blower Aeroacoustics Predictions Based on the Lattice Boltzmann Method", AJK2011-23018, AJK Conference, Hamamatsu, Japan.
- ⁴⁰ Pérot, F., Kim, M., Le Goff, V., Carniel, X., Goth, Y., Chassaignon, C., "Numerical Optimization of the Tonal Noise of a Centrifugal Fan Using a Flow Obstruction", Fan2012 International Conference, April 2012, Senlis, France.
- ⁴¹ Pérot, F., Moreau, S., Denner, M., Neal, D. and Kim, M., "Direct Aeroacoustic Prediction of a Low-Speed Axial Fan", AIAA paper 2010-3887, 2010.

- ⁴² Moreau, S., Henner, M., Brouckaert, J.F., Neal, D. "Numerical and Experimental Investigation of Rotor-Stator Interaction in Automotive Engine Cooling Fan Systems", 7th European Conference on Turbomachinery - Fluid Mechanics and Thermodynamics, Athens, March 2007.
- ⁴³ Gullberg, P. and Sengupta, R., "Axial Fan Performance Predictions in CFD, Comparison of MRF and Sliding Mesh with Experiments", SAE World Congress, 2011-01-0652.
- ⁴⁴ Pérot, F., Kim, M., Meskine, M., Freed, D., "NREL Wind Turbine Aerodynamics Validation and Noise Predictions Using Lattice-Boltzmann Method", submitted for 18th AIAA/CEAS Aeroacoustics conference, June 2012, Colorado Springs.
- ⁴⁵ Jeong, J. and Hussain, F., "On the identification of a vortex", J. Fluid Mechanics, vol. 286, pages 69-94, 1995.
- ⁴⁶ Casalino, D., Nötling, S., Fares, E., Van de Ven, T., Pérot, F., Brès, G., "Towards Numerical Aircraft Noise Certification. Analysis of a Full-Scale Landing Gear in Fly-Over Configuration", submitted for 18th AIAA/CEAS Aeroacoustics conference, June 2012, Colorado Springs.
- ⁴⁷ Pérot, F., Mann, A., Kim, M., Casalino, D., Fares, E., "Investigation of Inflow Condition Effects on the ANCF Aeroacoustics using LBM", submitted for Inter-Noise 2012, New York City.